Journal of Hydrology 381 (2010) 322–332

Contents lists available at ScienceDirect

Journal of Hydrology

journal homepage: www.elsevier.com/locate/jhydrol

Spatial variability of steady-state infiltration into a two-layer soil system on burned hillslopes

D.A. Kinner [a,*], J.A. Moody [b]

[a] Department of Geosciences and Natural Resources, Western Carolina University, Cullowhee, NC 28779, United States
[b] U.S. Geological Survey, National Research Program, 3215 Marine St. Boulder, CO 80309, United States

ARTICLE INFO

Article history:
Received 8 April 2009
Received in revised form 13 November 2009
Accepted 3 December 2009

This manuscript was handled by P. Baveye, Editor-in-Chief

Keywords:
Burned watershed
Ash
Infiltration
Overland flow

SUMMARY

Rainfall–runoff simulations were conducted to estimate the characteristics of the steady-state infiltration rate into 1-m^2 north- and south-facing hillslope plots burned by a wildfire in October 2003. Soil profiles in the plots consisted of a two-layer system composed of an ash on top of sandy mineral soil. Multiple rainfall rates (18.4–51.2 mm h^{-1}) were used during 14 short-duration (30 min) and 2 long-duration simulations (2–4 h). Steady state was reached in 7–26 min. Observed spatially-averaged steady-state infiltration rates ranged from 18.2 to 23.8 mm h^{-1} for north-facing and from 17.9 to 36.0 mm h^{-1} for south-facing plots.

Three different theoretical spatial distribution models of steady-state infiltration rate were fit to the measurements of rainfall rate and steady-state discharge to provided estimates of the spatial average (19.2–22.2 mm h^{-1}) and the coefficient of variation (0.11–0.40) of infiltration rates, overland flow contributing area (74–90% of the plot area), and infiltration threshold (19.0–26 mm h^{-1}). Tensiometer measurements indicated a downward moving pressure wave and suggest that infiltration-excess overland flow is the runoff process on these burned hillslope with a two-layer system. Moreover, the results indicate that the ash layer is wettable, may restrict water flow into the underlying layer, and increase the infiltration threshold; whereas, the underlying mineral soil, though coarser, limits the infiltration rate. These results of the spatial variability of steady-state infiltration can be used to develop physically-based rainfall–runoff models for burned areas with a two-layer soil system.

Introduction

Forest fires and post-fire hazards such as flooding and debris flows increasingly impact local populations with the continued expansion of the urban–wildland interface and have been exacerbated by recent drought conditions (2001–2003). Flooding, channel erosion (Krammes and Rice, 1963; Bolin and Ward, 1987; Moody and Martin, 2001a,b; Kinner and Moody, 2005; Moody and Kinner, 2006), debris flows, and sediment-laden flows (Eaton, 1935; Parrett, 1987; Cannon, 2001) are post-fire responses to even moderate or light rainfall intensities. Runoff (Anderson, 1974; Helvey, 1980; Bolin and Ward, 1987) and peak flows (Krammes and Rice, 1963; Anderson, 1974; Scott and van Wyk, 1990; Moody and Martin, 2001a; Veenhuis, 2002) after a wildfire must be accurately predicted before models of debris and sediment-laden flows can be developed. This requires a physical understanding of how fire changes soil properties, and thus, affects hillslope-infiltration and runoff generation processes.

Ash lies on top of the soil after a wildfire. Ash in the broad sense is a mixture of black carbon, soot, burned organic matter of various size that can include charred material, charcoal, and mineral material transported by the winds created by fire dynamics and deposited as combustion ceases (Jones et al., 1997; Trabaud, 1994). Ash and soil form a two-layer system, and ash may affect the infiltration and runoff response, particularly during the first few rain storms before it is washed away. The hydraulic role of ash in the runoff process has not been fully documented in the literature.

The literature provides little consensus on the impact of fire on steady-state infiltration rates. For example, steady-state infiltration rates on burned and unburned plots in Colorado (Benavides-Solorio and MacDonald, 2001) showed little difference, while measurements on other sites in Idaho, New Mexico and Colorado (Robichaud, 2000; Martin and Moody, 2001) indicated that the average steady-state infiltration rates decreased as burn severity increased. Fire-induced water repellency may be a process that reduces steady-state infiltration rate after a fire as well as in soils from unburned area (Dekker and Ritsema, 2000; Jarmillo et al., 2000). It may be extremely patchy, have different spatial scales (Cannon, 2001; Doerr and Moody, 2004), and cause the infiltration rate to be less than saturated hydraulic conductivity, K_s [L T^{-1}] (Wang

* Corresponding author.
E-mail address: dkinner@email.wcu.edu (D.A. Kinner).

0022-1694/$ - see front matter © 2010 Elsevier B.V. All rights reserved.
doi:10.1016/j.jhydrol.2009.12.004

et al., 2000). Water repellency of soils in burned areas has been shown to be related to temperature of soil heating, moisture content of the soils, the presence of organic material that coats mineral grains, and whether the soils were naturally water repellent (DeBano, 1981, 2000; Letey, 2001). Other explanations for a reduction in steady-state infiltration rate after fire may include surface sealing by ash and fine soil particles (Dunne and Dietrich, 1980; Römkens et al., 1990; Sumner and Stewart, 1992; Poesen, 1993; Onda et al., 2008), soil crusting (Rowe, 1948; Römkens et al., 1990; Imeson et al., 1992; Sumner and Stewart, 1992; Neary et al., 1999), and different soil properties between fine-grained ash and underlying coarse-grained soil layers (Ross, 1990; Lu and Likos, 2004; J. Godt, USGS, oral communication; Moody et al., in press). In any case, the essential variables for each process have a complex spatial distribution of soil patches that are probably determined by the vegetation distribution, but altered by variable heat impulses into the soil caused by the vagaries of a wildfire.

Runoff depends on the hydraulic characteristics of these soil patches and on the rainfall rate. Runoff generation after wildfires appears to be related to a rainfall rate threshold at the watershed scale (Inbar et al., 1998; Moody and Martin, 2001b,c; Kunze and Stednick, 2006; Moody et al., 2008). Infiltration-excess overland flow is frequently assumed to be the dominant process for burned areas (Wondzell and King, 2003; Shakesby and Doerr, 2006) and is produced when the rainfall rate, r [L T^{-1}] exceeds the steady-state infiltration rate, i_∞ [L T^{-1}], within a patch of soil. As r increases, the condition $r > i_\infty$ is met for an increasing number of patches on a hillslope (Dunne et al., 1991; Smith and Goodrich, 2000) and the contributing area to overland flow expands (Betson, 1964; Hawkins, 1982), but is probably less than the potential contributing or drainage area of a watershed. Because contributing area depends on rainfall rate, rainfall simulations using a single, high rainfall rates such as 80–100 mm h^{-1} may overestimate infiltration rates relative to simulations made at lower rainfall rates. The contributing area has seldom, if ever, been measured directly; it is often assumed, incorrectly, to be equal to the drainage area, and yet it is an essential variable for predicting runoff. In patches of soil where $r < i_\infty$, the steady-state infiltration rate is equal to r and these patches do not contribute to overland flow. Thus, the contributing area and the effective, spatially-averaged, steady-state infiltration rate, i_e [L T^{-1}], over a watershed will be functions of the spatial distribution of steady-state infiltration rates.

Hillslope ponding patterns reflect the spatial structure of the distribution of steady-state infiltration, which is equal to K_s for soils without water repellency. For example, if i_∞ increases as elevation decreases in a watershed, run-on increases, and the area of ponding increases more rapidly (Nachabe et al., 1997) than if i_∞ increases as elevation increases. In the former case, water is transmitted downslope over ponded patches as overland flow and rapidly saturates downslope, more permeable patches. The situation that predominates in a watershed would depend on whether coarse or fine material moves downslope into the channel; many channels in steep lands prone to burning have coarse material mantling the channels that may lead to increasing i_∞ with decreasing elevation. Some previous studies have assumed a random spatial distribution of K_s and have proposed exponential-distribution (Hawkins and Cundy, 1987) and lognormal-distribution models (Corradini et al., 1998; Smith and Goodrich, 2000). Thus, the relation between rainfall rate, steady-state infiltration rate, and runoff discharge will be a function of the spatial distribution of K_s or i_e (Morel-Seytoux, 1986).

Both natural soils and soils subjected to the heat of wildfires can be water repellent. The degree of water repellency depends on the heat imparted by the fire, the vegetation before the burn, and the organic compounds present in the soil. Water repellency can be extremely spatial variable (Doerr and Moody, 2004). Under some water repellent conditions, the infiltration rate less than K_s (Wang et al., 2000). Under these conditions, flow instability can cause fingering or attraction of water into larger, less water-repellent pores such that the water moves rapidly deeper into the soil profile. Infiltration rates appears to approach an asymptotically constant value i_∞, such that the long-time (30 min to hours) behavior is like a wettable or non water-repellent soil, but $K_s > i_\infty$. We report i_∞ rather than K_s because we do not know *a priori* the water repellency of the soils. If water repellency exists, field data would indicate an uneven wetting front and possibly an increase in infiltration with time.

Soil layering due to the presence of ash may also limit soil infiltration rates. In general, the ash appears to conduct water better than the underlying soil (Moody et al., 2009). This may be due to greater fire-induced water repellency on the coarse-grained material, or simply the difficulty of wetting coarser grained material due to low adsorption. The latter explanation is related to the well-known capillary barrier affect (Ross, 1990; Lu and Likos, 2004), whereby moisture-dependent hydraulic conductivity is lower for sands than clay at low moisture content. If the fine-grained material sits over the coarse-grained material than water will often pond on the interface between the two layers and not enter the coarse-grained layer because of low hydraulic conductivity.

In this study, we conducted a series of rainfall simulations with variable rainfall rates to produce steady-state runoff from 1-m^2 plots on north- and south-facing burned hillslopes, which had a two-layer system of an ash layer on a soil layer. We measure infiltration at this scale because it integrates some of the variability measured by instrumentation (permeameters) at smaller scales, but it does not integrate the routing affects that control infiltration at the larger scales. We are effectively measuring infiltration instead of the combined behavior of infiltration rates and routing. The purpose of this paper is: (1) to provide estimates of the mean and variance of the spatial distribution the steady-state infiltration for such a two-layer system, (2) to estimate the contributing area within 1-m^2 plots, and (3) to determine the effects of the ash on the spatially-averaged steady-state infiltration rate.

Spatial variability of infiltration

Rainfall simulation is useful in that it allows soils to reach a steady-state runoff and infiltration rates. The results from the simulations can be used to estimate the character of the spatial variability of the steady-state infiltration rates and the rainfall threshold below which no overland flow is produced. Hawkins (1982) recognized that the relation of rainfall rate to runoff rate at plot and small watershed scale is linked to the spatial variability of infiltration rates, which he refers to as "effective" infiltration rates. To simplify the development of theoretical spatial distribution models of infiltration, he assumed no runoff–runon phenomena, and thus, the interaction between runoff and infiltration identified and modeled by others (Nachabe et al., 1997; Corradini et al., 1998; Fiedler and Ramirez, 2000) is ignored in the treatment below.

The underlying spatial distribution of patches of soil with differing values of steady-state infiltration, i_∞, in an experimental plot is unknown *a priori*. Therefore, theoretical spatial distributions models of i_∞ can be used to estimate the spatial distribution in the field. The spatial-averaged steady-state infiltration rate, i_e, of an area with a spatially variable infiltration rate can be calculated by:

$$i_e = r\{1 - F[i_\infty(r)]\} + \int_0^r i_\infty f(i_\infty) di_\infty \quad (1)$$

where $F[i_\infty(r)]$ is the cumulative distribution function (*cdf*) of i_∞ evaluated for a given rainfall rate, r, and $f(i_\infty)$ is the probability density function (*pdf*) of i_∞ (Morel-Seytoux, 1986; Smith and Goodrich, 2000). The first component of Eq. (1) represents soil patches that allow infiltration at a rate equal to r because the rainfall rate is less than the infiltrability of the soil at these locations ($r < i_\infty$ for the steady case). The second component of Eq. (1) represents the average i_∞ for the area for which $r > i_\infty$. By using different spatial distribution models for $f(i_\infty)$ in Eq. (1), relations between r and i_e can be obtained. In the case of a two-layered system, i_e is the spatially-averaged, two-layered, steady-state infiltration rate.

Threshold

This model was selected because the literature reports observed rainfall-rate thresholds for runoff after wildfire at watershed scales. It assumes that once a rainfall rate threshold is crossed, a patch or plot produces runoff. Thus, i_∞ is a constant over the entire plot such that:

$$F(i_\infty) = \begin{cases} 0 & r \leqslant i_{\text{threshold}} \\ 1 & r > i_{\text{threshold}} \end{cases} \tag{2}$$

where $i_{\text{threshold}}$ is the steady-state infiltration threshold. This also assumes that the maximum contributing area is equal to the entire plot area. Therefore, this simple model was modified to model partially contributing area so that the contributing area, a_c [nondimensional] is equal to the fraction of the entire plot area contributing runoff. The *cdf* has the form:

$$F(i_\infty) = \begin{cases} 0 & r \geqslant i_{\text{threshold}} \\ a_c & r > i_{\text{threshold}} \end{cases} \tag{3}$$

If $r > i_{\text{threshold}}$, the relation between the unit discharge, q [$\mathrm{L\,T^{-1}}$] and r is:

$$q = a_c(r - i_{\text{threshold}}) \tag{4}$$

Lognormal

This model was selected because it fits many field measurements (Smith and Goodrich, 2000) and has the following *cdf*:

$$F(i_\infty) = \frac{1}{2} + \frac{1}{2} Erf\left[\frac{\ln(i_\infty) - E_i}{\sigma\sqrt{2}}\right] \tag{5}$$

where *Erf* is the error function, E_i the expected value of $\ln(i_\infty)$, and σ is the standard deviation of $\ln(i_\infty)$. The corresponding *pdf* is:

$$f(i_\infty) = \frac{1}{i_\infty \sigma\sqrt{2\pi}} \exp\left[\frac{(\ln(i_\infty) - E_i)}{2\sigma^2}\right] \tag{6}$$

The following empirical relation then holds between q and r:

$$q = r - E_i\left[1 + \left(\frac{E_i}{r}\right)^p\right]^{\frac{-1}{p}} \tag{7}$$

where the empirical constant, p, is computed as:

$$p = \frac{1.8}{(CV_i)^{0.85}}, \tag{8}$$

and CV_i is the coefficient of variation of the lognormal distribution of i_∞ (Smith and Goodrich, 2000).

Study site

The Overland Fire started near Jamestown, Colorado, on 29 October 2003, migrated east over a single day, burned nearly 16,000 hectares, and was extinguished the same day by a rain-snow storm. The fire burned after the summer convective rainstorm season, so ash remained on the slope. Ash still blanketed the slopes in the spring, and to preserve this ash, we covered the experimental plots with tarps and diverted overland flow around the plots.

Rainfall simulations were conducted in 1-m^2 plots on north- and south-facing hillslopes. Each aspects have distinct soils types (Birkeland et al., 2003), vegetation, and geomorphic characteristics (Moody and Martin, 2001a; Moody and Kinner, 2006). Geology under both hillslopes is Precambrian pegmatite on ridges, Silver Plume Monzonite on side slopes, and colluvium in the stream valleys (Brandt et al., 2003). Two plots were established at random locations on the north-facing (plot N13 and N15) and two plots on the south-facing (plot S13 and S15) hillslope (Fig. 1). Vegetation on the north-facing slope included aspen (*Populus tremuloides*) on the lower slope and Douglas fir (*Pseudotsuga menziesii*) near the top of the upper slope. Ponderosa pine (*Pinus ponderosa*) was the dominant species on the south-facing slope.

Post-fire soils consisted of layers of ash, burned or unburned litter and duff, and sandy soil. Some areas included all three layers, and others had only sandy soil. Surface soil samples (3-cm deep) were collected within the south-facing hillslope grid (Fig. 1) and were generally coarser (average median diameter $\overline{D_{50}} = 0.88$ mm; $n = 72$) than the surface soil samples from the north-facing hillslope grid ($\overline{D_{50}} = 0.66$ mm; $n = 81$). Ash depths on the upper and lower slopes of both aspects ranged from 10 to 15 mm. Mean diameter of the ash was 0.35 mm ($n = 2$) in the north facing experimental plots and 0.92 mm for ($n = 4$) in the south-facing experimental plots. Partially-combusted needles dominated the ash layer in plot S13.

All plots had some drainage network with multiple flow paths (Fig. 2). Those in the south-facing slope plots had well-defined rills or flow paths prior to the rainfall simulations, which had been cut earlier through the ash layer and into the sandy soil. Those on the north-facing slope were not incised and appeared to be more dendritic. The flow paths in all plots were ordered by using Horton–Strahler stream ordering system and the stream numbers and path lengths were similar for all plots (Kinner and Moody, 2008; Table 5 and Figs. 15–18).

Methods

Rainfall simulations

A single-nozzle rainfall simulator was developed to produce multiple rainfall rates by using three different interchangeable nozzles and different water pressures. Calibration of the rainfall simulator on a flat surface, gave rainfall rates (over a 1 m^2 area) of approximately 20, 35, and 45 mm h^{-1} (rainfall coefficient of variation, $CV_r < 0.17$). We measure infiltration at this scale because it integrates some of the variability measured by instrumentation (permeameters) at smaller scales, but it does not integrating the routing affects at the larger scales. We are effectively measuring infiltration instead of the combined behavior of infiltration rates and routing. Field measurements used rainfall rates ranging from 18.4 to 51.2 mm h^{-1} on each plot to determine the relation between i_e and r (Table 2). Three tipping-bucket recording rain gages were deployed along the outside edge of the plot (at the top, middle, and bottom), and small visual rain gages were installed outside the plot at each corner to record total rainfall during each simulation run (Kinner and Moody, 2008). These rainfall rates are similar to the 1- to 5-year recurrence intervals common in the western United States (Hershfield, 1961).

Two types of rainfall simulations were conducted. The first type was a series of 14 short-duration simulations (~30 min) on south-facing (8 simulations) and north-facing slopes (6 simulations) to examine the impact of rainfall rate on effective infiltration rates.

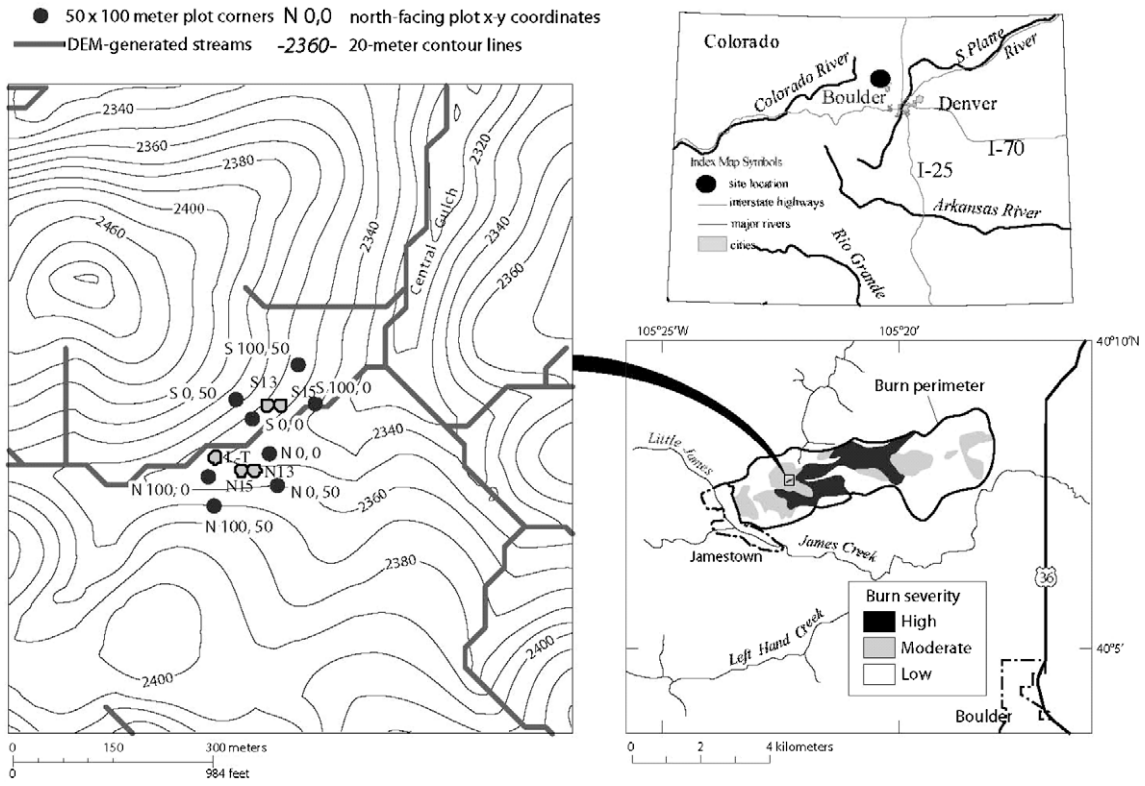

Fig. 1. Site of rainfall simulation plots within the Overland burn area. Upper right: Site location relative to some of the major cities, rivers, and highways in Colorado. Lower right: Burn perimeter with the burn severities (compliments of Eric Schroder, US Forest Service). Upper left: Location of the short duration plots (S13, S15, N13, and N15) on north- and south-facing hillslopes, and the long-term plot L-T, on the north-facing slope. Plots were randomly selected from among 50 plots within a 50 m by 100 m grid indicated by the black circles. Shaded circles represent the approximate rainfall plot locations.

These were conducted over a 2-week period for the south-facing slopes, and over a 2-day period for the north-facing slopes during the late summer and early fall of 2004 (Table 1). Discharge was collected in a container at the base of the plot at 1 min intervals for 30 min. The rainfall, runoff, soil moisture, plot topography, overland flow runoff velocities, and the depth of the surface ash layer were measured in all four plots. Details of the methods, the data processing procedures, discharge hydrographs, and ancillary data (soil moisture, flow-path velocities, suspended sediment, stratigraphy, and topography) are reported by Kinner and Moody (2008). The second type of was a pair of long-duration rainfall simulations (181 and 219 min respectively) to measure the subsurface response of the soils (vertical moisture movement) during prolonged rainfall. This response was measured in a separate plot on the north-facing hillslope by using a steady rainfall rate of 16.9 mm h^{-1}, which was continuous except when the generator powering the simulator needed to be refueled. Tensiometers measured matric suction in a single vertical profile at depths of 2, 2.5, 6, 10, and 21 cm below the soil surface.

Data analysis

The measured runoff discharge and rainfall rates were used to compute the observed spatial-averaged steady-state infiltration rates for each plot. This observed effective infiltration rate, i_e^o [$L\,T^{-1}$], was calculated as:

$$i_e^o = r - \frac{Q}{A} = r - q^o, \tag{9}$$

where Q [$L^3\,T^{-1}$] is the observed steady-state discharge from the plot at 1-min intervals, q^o [$L^3\,T^{-1}$] is the observed runoff discharge, A [L^2] is the plot area ranging from 0.91 to 0.94 m^2. This form of Eq. (9) is the same as that published by Dunne et al. (1991) with different symbols. Continuous runoff hydrographs were obtained by fitting a cubic spline to q^o. Each continuous hydrograph was divided into a period of time corresponding to a transient state (hydrograph rise) and a period of time corresponding to a steady state. We define the time-to-steady state, t_{steady} [T], to be the time when the derivative of the hydrograph, $\frac{dq^o}{dt}$, is 0 or first becomes negative (Fig. 3 and Table 1).

A theoretical spatial-averaged steady-state infiltration rate, i_e was computed by using the two spatial distribution models of i_∞ (Eqs. (3)–(8)). The theoretical steady-state unit discharge, q^t, was equal to $r - i_e$. For each model, the fit between the theoretical steady-state discharge and the observed steady-state discharge was optimized by adjusting model parameters and minimizing the sum of square errors (SSE) between the theoretical discharge and the observed discharge (Table 1). For the threshold model, the expected or spatial mean value of the steady-state infiltration rate, E_i was adjusted; for the modified threshold model, the fraction of the contributing area, a_c and E_i were adjusted; and for the lognormal model, E_i and CV_i were adjusted.

In order to increase the number of observations, all the north-facing ($n = 6$) and south-facing ($n = 8$) rainfall simulations were grouped by aspect. This grouping had the advantages of providing a general relation between i_∞ and r for north- and south-facing slopes.

Results

Rainfall

Simulated rainfall rates were essentially constant with time. Ten of the 14 short-duration simulations did not have a statistically

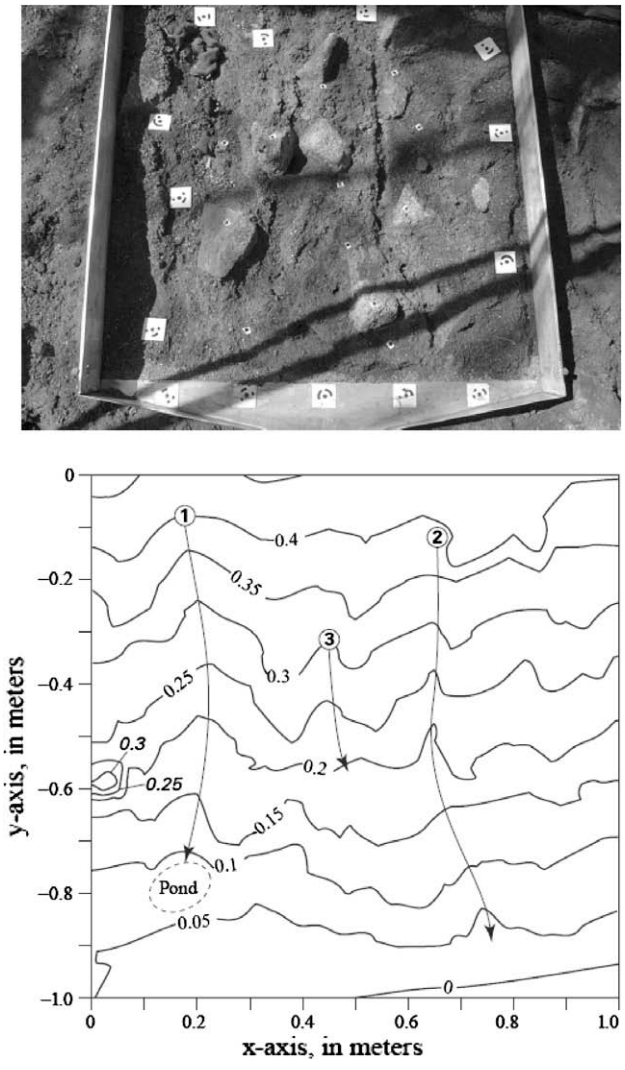

Fig. 2. An example of an experimental plot (plot N13) with a photograph above and the topographic map (in m) below. The numbers in the plot refer to main water flow paths during plot hydrologic response.

significant linear change in rainfall rate with time. The maximum rate of change during a simulation experiment was 0.31 mm h^{-1} min^{-1}, and the coefficient of variation (*CV*) of 2 min rainfall intensities ranged from 0.04 to 0.16. Simulated rainfall was more variable in space. The downhill tipping-bucket recording rain gage near the plot outlet typically recorded the lowest rainfall rate of the three gages along the plot margin. The downhill tipping bucket gage is the farthest from the nozzle of the three gages because the soil surface is tilted. It therefore receives the least amount of rainfall because the spray spreads out with vertical distance. The *CV* for the three tipping-bucket rain gages varied from 0.08 to 0.36 during calibration runs for the three different rainfall rates (Kinner and Moody, 2008; Table 3). The *CV* for the spatial distribution of rainfall rates (downslope variability) during the short-duration simulations was 0.32, and cross-slope variability based on visual gages (average percent difference between total rainfall on the left and right side of the plots) was 0.17 (Kinner and Moody, 2008; Tables 3 and 4).

Short-duration rainfall simulations

The two-layer system (ash over sandy soil) produced ponding and steady-state overland flow. Average soil moisture at the surface (0.00–0.05 m) in the north-facing plots increased from 0.37 to 0.40 g g^{-1} and from 0.10 to 0.19 g g^{-1} in the south-facing plots. At a depth of 0.20–0.25 m the average soil moisture was nearly constant throughout the simulations increasing from 0.20 to 0.22 g g^{-1} and from 0.13 to 0.19 g g^{-1} in the north- and south-facing plots, respectively (Kinner and Moody, 2008). Average time-to-steady state, t_{steady} was 11 min in the north-facing plots with an average initial soil moisture of 0.37 g g^{-1}; whereas, in the south-facing plots (initial soil moisture was 0.10 g g^{-1}) and the average t_{steady} was 15 min. Steady-state unit discharge increased from an average of 2.7 mm h^{-1} for r = 21.7 mm h^{-1} (simulations 7, 8, 9, and 11) to a unit discharge of 27.7 mm h^{-1} for r = 48.1 mm h^{-1} (simulations 2, 3, 13, and 14 in Table 1).

Long-duration rainfall simulations

In the long-duration experiments (Figs. 4 and 5), the tensiometer data (Fig. 4) show a downward moving pressure wave. The wave reaches the 0.06–0.10 m zone within the first 40 min of simulation 15 (Fig. 4A) and in less than 30 min for simulation 16 (Fig. 4B). At each of these depths, the soil appears saturated (matric suction ~0 cm), or to be approaching saturation.

Spatial-averaged steady-state infiltration rates

The observed spatially averaged steady-state infiltration rates, i_e^o, were essentially constant across the range of rainfall rates measured in the field. Mean observed rates were 20.8 mm h^{-1} and 24.2 mm h^{-1} in the north- and south-facing plots respectively. Estimates of the expected, E_i, or mean value of the spatial distribution of i_e^o using three theoretical models (Eqs. (3)–(8)) were similar to the observed values. They were 20.8, 19.2, and 22.2 mm h^{-1} for the threshold, modified threshold and lognormal models for the north-facing plots and similarly 24.2, 19.6, and 26.1 mm h^{-1} for the south-facing plots. This type of analysis of rainfall simulation data also provides additional estimates of the characteristics of the steady-state infiltration rate. The lognormal model provided estimates of the variability of the spatial distribution, which were CV_i = 0.40 and 0.11 for the north- and south-facing plots respectively (Table 2). The modified threshold model provided estimates of the contributing area a_c, (0.90 and 0.74) as well as estimates of the rainfall or infiltration threshold rate, $r_{threshold} = i_{threshold}$ (19.2 and 19.6 mm h^{-1}) required to produce runoff from the north- and south-facing plots.

Discussion

Rainfall rates used in these simulations were typical of storms with 1- to 5-year recurrence intervals and thus provide useful estimates of the time-to-steady state runoff for modeling purposes of a two-layer system of ash on top of sandy soil. The times to steady state are essentially the same for the north- and south-facing plots (11 and 15 min). These values of t_{steady} for the two-layer system were slightly greater than the average values (8 min) scaled from six measurements published by Benavides-Solorio and MacDonald (2001, Fig. 3) for areas affected by wildfire, and those values (3–5 min) estimated from Fig. 2 presented by Robichaud (2000) for areas affected by prescribed fire. However, their simulated rainfall rates (66–94 mm h^{-1}) were substantially greater than those used in this study and the amount of ash on the surface is undocumented. The greater rainfall rates may shorten the time-to-steady state, or alternatively, the effect of the layer of ash may be to slightly increase the time-to-steady state. Runoff from this two-layer system depends on the spatial distribution of the steady-state infiltration rates, which is affected by the ash layer.

Table 1
Summary of rainfall and hydrologic data for rainfall simulations.

Simulation number	Plot		Surface[a] soil moisture			Time-to steady state, t_{steady} (min)	Rainfall rate, r (mm h^{-1})[d]	Observed steady-state unit discharge, q^o (mm h^{-1})	Observed spatially averaged steady-state infiltration rate i^o [e] (mm h^{-1})	Runoff ratio
	ID	Area (m^2)[b]	Initial (g g^{-1})[c]	Final (g g^{-1})	Difference (g g^{-1})					
Short-duration rainfall simulations										
North-facing plots										
9	N13	0.93	0.27	0.27	0.00	17	23.3	5.1	18.2	0.22
10	N13	0.93	0.27	0.52	0.25	10	34.0	15.5	18.5	0.46
11	N15	0.91	0.66	0.42	−0.24	16	24.9	4.3	20.6	0.17
12	N15	0.91	0.42	0.45	0.03	8	35.3	11.5	23.8	0.33
13	N15	0.91	0.39	0.42	0.03	9	47.4	24.9	22.5	0.53
14	N13	0.93	0.25	0.35	0.10	7	51.2	29.9	21.3	0.58
South-facing plots										
1	S13	0.90	0.09	0.19	0.10	19	46.2	17.9	28.3	0.39
2	S15	0.92	0.06	0.15	0.09	13	48.2	28.1	20.1	0.58
3	S15	0.92	0.16	0.21	0.05	8	45.7	27.8	17.9	0.61
4	S13	0.90	0.13	0.23	0.10	11	49.2	13.2	36.0	0.27
5	S13	0.90	0.08	0.21	0.13	26	37.1	9.4	27.7	0.25
6	S15	0.92	0.06	0.15	0.09	18	34.0	7.5	26.5	0.22
7	S15	0.92	0.09	–	–	13	20.0	1.3	18.7	0.07
8	S13	0.90	0.14	0.17	0.03	NR	18.4	0.0	18.4	0.00
Long-duration rainfall simulations										
15	$N_{longdur}$	0.95	–	–	–	14	16.9	7.7	9.2	0.46
16	$N_{longdur}$	0.95	–	–	–	16	16.9	3.9	13.0	0.23

[a] Surface is 0.00–0.05 m.
[b] m: meters.
[c] g: grams.
[d] h: hour.
[e] NR: no runoff.

Spatial distribution of steady-state infiltration rates

The relation between rainfall rate and runoff discharge provides an estimate of the spatial distribution of steady-state infiltration rates. Spatially-averaged steady-state infiltration rate changes as r increases because new patches are being incorporated into the contributing area. The estimates of i_e for the north-facing plots had less variability (Table 2: SSE = 15.6–23.5 mm^2 h^{-2}), which reflects the similarity in surface characteristics of the two north-facing plots. The south-facing plots had two different surface materials with "fine" ash on plot S15 and "coarse" ash on plot S13, with the latter composed of coarse needles that appeared to adsorb more water (0.16–0.19 g-water per mm-ash).

Field observations, in addition to the simulation measurements, suggest that infiltration variability is more complicated than that predicted by the simple lognormal models (Eqs. (5)–(8)) used in this paper. Generally, ponding was observed, as early as the first minute, in the topographic lows and along flow paths of the drainage network. As the rainfall continued, more patches with ponded water were observed, some became connected, and more flow paths delivered water to the outlet. Sometimes ponding was initiated in the center of a flow path and expanded its way both upslope and downslope. Other observations indicate a non-slope dependent wetting pattern. For plot N13, water flowed into a patch representing a topographical depression or surface sink (such as created by burned roots) near the center of the plot and did not reach the plot outlet. Therefore, this runoff (and part of the i_∞ distribution) was not measured at the plot scale. The variability of the rainfall rate affects the calculation of the spatial distribution of i_∞. Lower parts of the plots sometimes received less rainfall which meant that ponding and connection between patches took longer. However, the lower rainfall rates at the base of the plot were likely compensated by run-on processes from the upslope end of the plot that are not accounted for in these simple models. In summary, the calculation of an empirical distribution of i_∞ is a function of the spatial distribution of i_∞, the connectivity pattern of flow paths, and the variability of the rainfall rate.

A rainfall rate threshold for burned areas in the western mountains appears to be emerging in the literature. This threshold expressed as a 30-min average rainfall intensity is about 10 mm h^{-1} (30 min rain intensity) for the initiation of runoff at watershed scales of 1–100 km^2 in granitic terrain (Doehring, 1968; Inbar et al., 1998; Moody and Martin, 2001a,c; Kunze and Stednick, 2006; Moody et al., 2008) and at smaller watersheds of about 0.5 km^2 in volcanic terrain (Moody et al., 2008). Note that for burned areas in California, it appears that the threshold for watershed response may be lower. The threshold has not been established at smaller scales (1–10 m^2). Many of these reported measurements have been for soils where the ash has been removed by wind or water. The rainfall rate threshold in this study with the presence of ash was modeled explicitly by the modified threshold distribution models, which gave values of $i_{threshold}$ equal to 19.2 and 19.6 mm h^{-1} (Table 2) or about twice that for the watershed scale (0.5–100 km^2). This threshold was captured implicitly by the lognormal distribution model by the point of maximum curvature for the lognormal curve (Fig. 6). This point is approximately 19.0 mm h^{-1} for the north-facing plots and 26 mm h^{-1} for the south-facing plots. These values are also about twice that for the watershed scale, but similar to those estimated by using the two threshold models.

Our estimates of the rainfall rate threshold are about twice those reported for the watershed-scale without ash (10 mm h^{-1} for 1–100 km^2 watersheds as cited above) that are based on measuring rainfall and discharge data. One would expect the threshold to decrease as the spatial scale decreases because fewer sinks are present. The increase in the rainfall rate threshold is then counter-intuitive, but suggests that the cause may be the layer of ash, which can absorb substantial amounts of water. Scaling issues may come into play here as well, because we are comparing instantaneous rainfall intensities at the plot scale with I_{30} at the small

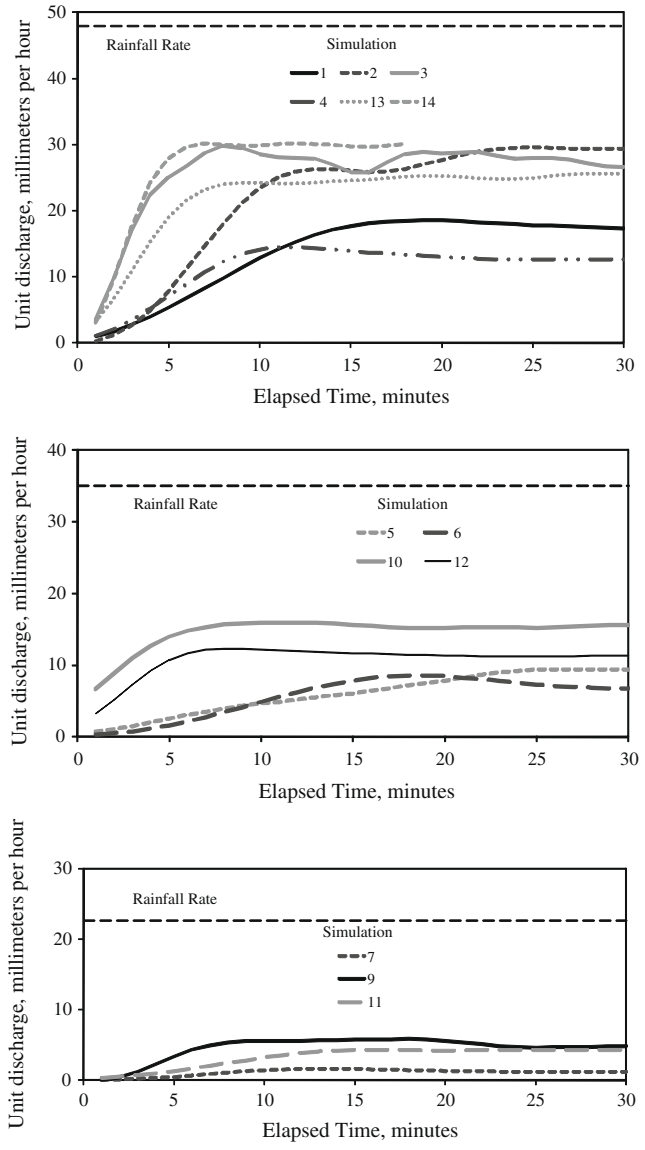

Fig. 3. Unit discharge hydrographs for 14 rainfall simulations. A cubic spline was used to smooth the hydrograph. The rainfall rate is shown as a dashed line near the top of each graph.

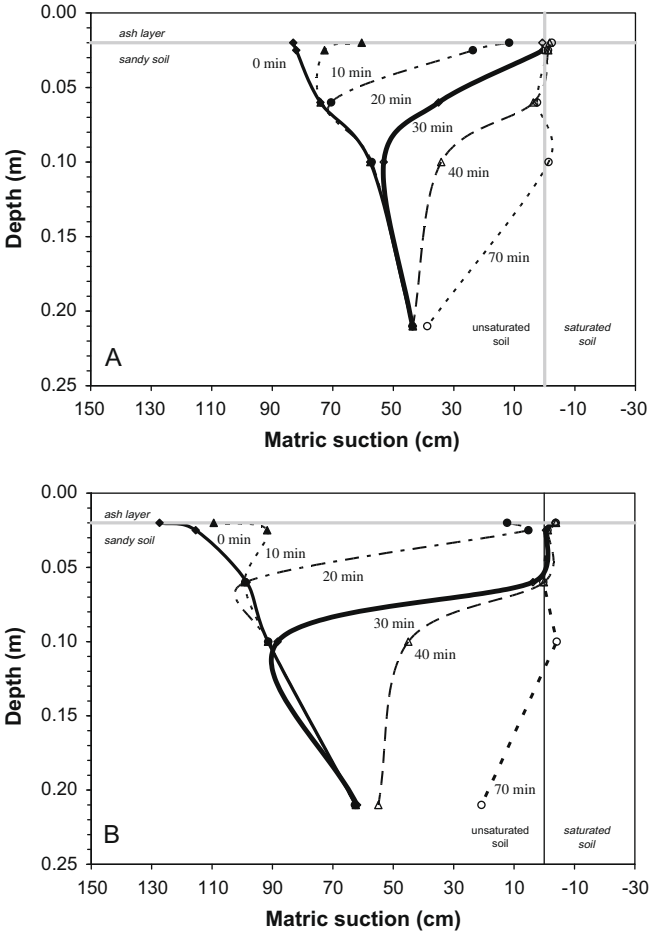

Fig. 4. Matric suction profiles associated with different times from start of the long duration simulations. (A) Experiment 1 and (B) Experiment 2.

watershed scale. It is likely that the instantaneous threshold at the watershed scale is higher than 10 mm h^{-1} but becomes lower when averaged over a half hour period. Alternatively, lower infiltration rate patches may be present at the larger spatial scales which are not present in our measured plots.

The use of spatially variable distribution models to estimate the characteristics of i_∞ may provide a key to scaling up plot and hillslope measurements to watershed scales. Smith and Goodrich (2000) indicate that using a rainfall-dependent, saturated hydraulic conductivity affects simulation results at both the plot and watershed scales. Clearly, the idea of using a single i_∞ in a model will be inadequate for simulating the range of storms after a wildfire. Rather, it seems that an approach that estimates the underlying spatial distribution of i_∞, like the one pursued here, would be more realistic and must include the effects of connectivity of drainage networks on i_e. Soil infiltration properties of patches and the connectivity of these patches along a surface flow path may control the threshold. For example, Moody et al. (2008) defined a new variable (hydraulic functional connectivity) which incorporated the order of burn severity patches along hillslope flow paths (at the coarse scale of 30-m × 30-m patches). This metric of hydraulic functional connectivity moderately improves the prediction of peak runoff response from watersheds. Thus, this unknown issue of how connectivity of hydrologic flow paths at the hillslope scale influence the spatial-averaged estimates of i_∞ needs to be investigated.

Effects of ash

Steady-state infiltration rates

The values of the steady-state infiltration rate calculated for our simulations are similar to others studies using different rainfall rates. The range (17.9–36.0 mm h^{-1}) corresponds to rainfall rates lower than those reported in other studies. Therefore, to compare our values with published values we used the lognormal model (Eqs. (5)–(8)) to extrapolate our observations to higher rainfall rates. This extrapolation indicates that the values are similar to, but are generally lower than, other observed values reported for Colorado soils without an ash layer (Fig. 7). One explanation is that ash may block entry into the surface of mineral soil by filling up pores. Another explanation is that water is attracted to ash particles and not the sandy subsurface layer, such that the downward movement of water is restricted. Moreover, the values of i_e (Fig. 7, burned or unburned from rangeland and multiple types of forest) fall within a range of less than one order of magnitude. This contrasts with soil saturated hydraulic conductivities reported in the literature for unburned area, which can range over several orders of magnitude. The consequence of this narrow range of i_e

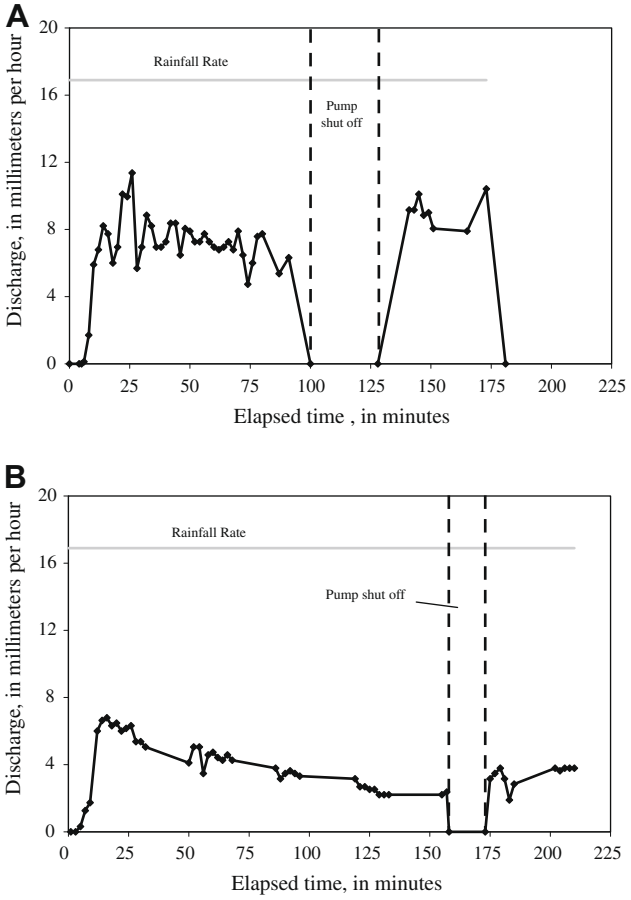

Fig. 5. Hydrographs for the long-duration simulations. Dashed lines indicate the periods when the rainfall simulation was paused during: (A) Experiment 1 and (B) Experiment 2.

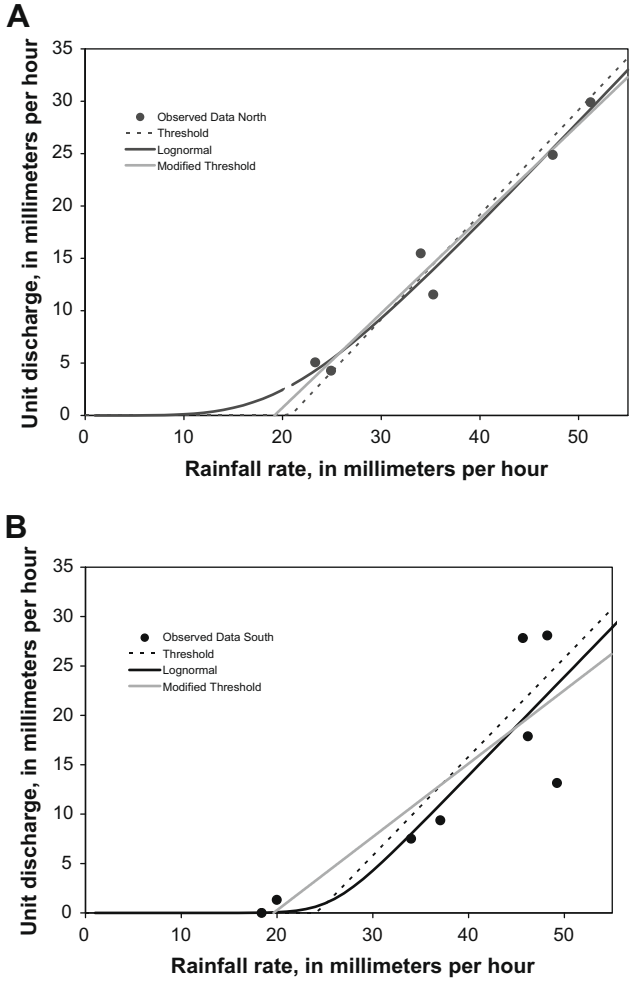

Fig. 6. Comparison between observed data from rainfall rate and steady-state unit discharge and three spatial distribution models for spatially-average, steady-state infiltration rate i_e. (A) North-facing hillslope. (B) South-facing hillslope.

means that a slight difference in steady-state infiltration rates can shift the rainfall–runoff process back and forth across the threshold condition ($r = i_\infty$), which would produce substantial differences in runoff.

Hillslope aspect differences

Despite differences in moisture content, bulk density (1.1 g/cm^3 for the north facing-slopes; 1.2 g/cm^3 for the south facing slopes) and ash texture (Kinner and Moody, 2008; south-facing ash $\overline{D_{50}} = 0.92$ mm; north-facing $\overline{D_{50}} = 0.35$ mm) on the north- and south-facing hillslopes, the responses of all of the plots were similar except plot S13 with the course needles in the ash layer. The two hydrograph for this plot at the highest rainfall rate (46.2 and 49.2 mm h^{-1}; Table 1) had longer values of t_{steady} (simulations 1

Table 2
Estimates of spatial distribution characteristics of steady-state infiltration rate for a two-layer system of ash on top of sandy soil.

Theoretical model	Spatially-averaged steady-state characteristics					
	E_i [a] (mm h-1)[g]	CV_i [b]	a_c [c]	$r_{threshold}$ [d] (mm h^{-1})	SSE[e] (mm^2 h^{-2})	R^2 [f]
North-facing plots						
Threshold 20.8	–	1.00	20.8	23.5	0.97	
Modified threshold	19.2	–	0.90	19.2	17.2	0.97
Lognormal	22.2	0.40	1.00	19.0	15.6	0.97
South-facing plots						
Threshold	24.2	–	1.00	24.2	297	0.73
Modified threshold	19.6	–	0.74	19.6	225	0.73
Lognormal	26.1	0.11	1.00	26.0	213	0.74

[a] E_i: expected mean infiltration rate.
[b] CV_i: coefficient of variation in infiltration rate.
[c] a_c: contributing area as a fraction of the whole.
[d] SSE: sum of squared errors.
[e] $r_{threshold}$.
[f] R^2: sum of squared errors.
[g] mm: millimeters; h: hour.

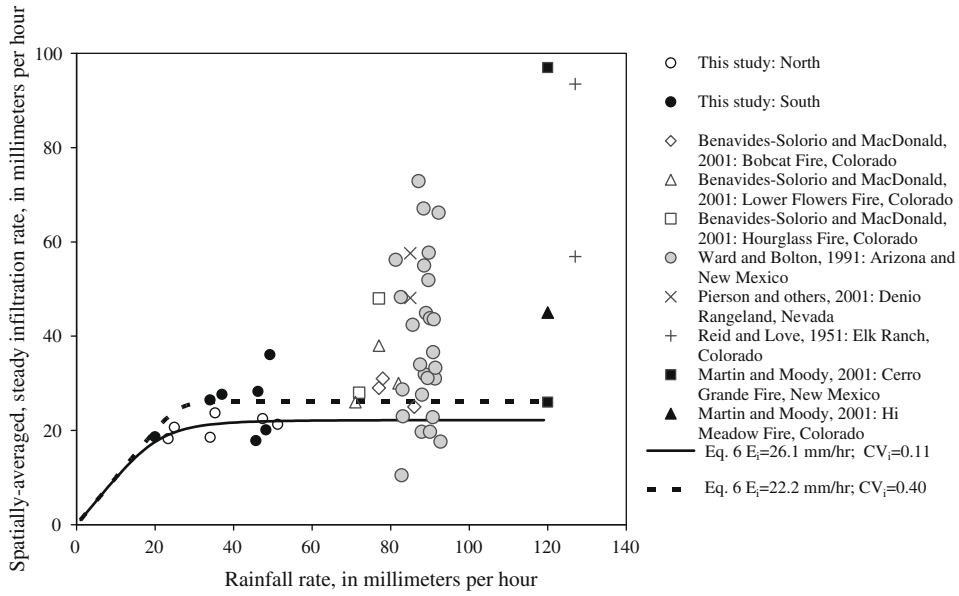

Fig. 7. Measurements of spatially-averaged, steady-state infiltration rates for burned and unburned plots in the western United States. Most plots probably had various amounts of ash, and most probably had no continuous layer of ash. Data from this study is for a two-layer system of ash on top of mineral sandy soil.

and 4, Fig. 3) and lower steady-state discharge. Also, no flow reached the plot outlet at the lowest rainfall rate (18.4 mm h^{-1}; Table 1). Thus, the presence of the course needles on the south slope appears to be the cause for the increase of i_e^o (28.3 and 36.0 mm h^{-1}, respectively).

Water repellency

Water repellency may influence the form of the discharge hydrographs. All hydrographs fluctuated around a more or less constant value. Of particular interest are the hydrographs for simulations 4, 6, and 7 that decreased with time (Fig. 3, Table 2). The steady-state discharge decreased 13%, 21%, and 28% respectively from the peak value, which is greater than the experimental error (5%). This discharge decrease corresponds to an increase in i_e. Such a decrease and then an increase in infiltration rate may be caused by water repellency (see Fig. 2, Type 3, Imeson et al., 1992). This same pattern was identified by Robichaud (2000) and Wang et al. (2000) during rainfall simulations on water-repellent soils and into soils with trapped air by Wang et al. (2000). A proposed mechanism for this increase in infiltration with time is attributed to the partial or complete breakdown of the initial water repellency caused by the solubility of water repellent compounds (DeBano, 1981). Little is known about the time scales for the breakdown of water repellency (Doerr et al., 2000), which may be <1 h (Doerr and Thomas, 2000), to several weeks (Crockford et al., 1991), or to no breakdown after 30 days (Doerr and Thomas, 2000). The breakdown is not necessarily permanent, as the soil may or may not become water repellent if soil moisture content is reduced (Doerr and Thomas, 2000). Once a critical moisture threshold (MacDonald and Huffman, 2004) or pressure (Wang et al., 2000) is surpassed, the soil will wet and the infiltration rate will increase. Notably, in our simulations the possible breakdown of water repellency is suggested by only a few simulations. In the other hydrographs, water repellency, if it exists, may breakdown during the rising hydrograph (<7–26 min) or at times greater than the length of the simulations (>30 min).

Two-layer system

The two-layered pressure profile indicates that the ash and soil are wettable. Smith (1990) discussed the pressure distribution at steady state for a two-layered system with a uniform initial pressure profile and showed that if the saturated hydraulic conductivity in the upper layer, K_{s1}, limits infiltration (i.e. $K_{s1} < K_{s2}$), then the pressure at the interface between the upper layer (subscript $s1$) and the lower layer (subscript $s2$) is less than saturated. Conversely, if $K_{s1} > K_{s2}$, then the lower layer controls infiltration and pore pressure is positive as water ponds from the interface to the surface. The tensiometer record suggests that the top of the lower layer is saturated meaning little or no pressure gradient in the upper ash layer. This implies that either $K_{s1} > K_{s2}$ or that the ash layer (10–15 mm thick) is too thin to affect the flow (Smith, 1990). Thus, ash appears to store water rather than control infiltration. The tensiometer observations were made under relatively wet conditions, and the response may differ under dry conditions directly after a fire.

The results of the infiltration experiments are consistent with the behavior of a capillary barrier, specifically the likelihood that $Ks_1 > Ks_2$. However, this relation is only true for a capillary barrier under dry conditions, and the conditions were quite moist at the time of the experiment. Thus, ash appears to conduct water better than the underlying soil under moist conditions which is consistent with the experimental data of Moody et al. (2009) who showed that $K_{ash} > K_{burned\_soil}$ (their natural soil in Table 2; at −6 cm of tension) for two sets of particle sizes. Again, these field experiments cannot fully resolve the relations between the two layers because the ash layer is too thin to get pressure measurements within the ash.

The tensiometer data do not specifically resolve the type of overland flow. However, the data indicate that the ash is wettable and a wetting front moves steadily into the soil. A shallow saturation excess overland flow that is generated by ponding on the ash soil interface is possible as is the potential that the system is infiltration-excess overland flow. After the initial ponding, infiltration is clearly controlled by the lower layer of soil because the zone of saturation moves steadily down through the soil, so for much of the time it is infiltration excess. Work by Onda et al. (2008) in Northern California indicates that shallow saturation excess overland flow in an ash layer may ultimately evolve to infiltration overland flow. The only way to resolve whether the ponding occurs first at the bottom of the ash layer and moves up to the surface is to embed a tensiometer in the

first millimeter of soil. This is difficult without completely disturbing the soils.

Conclusions

A rainfall simulator using multiple rainfall rates ranging from 18.4 to 51.2 mm h^{-1} generated overland flow from 1-m^2 plots on burned hillslopes with a two-layer system of ash on top of sandy soil. The time to steady-state discharge ranged from 7 to 26 min. Observed spatially-averaged, steady-state infiltration rates ranged from 18.2 to 23.8 mm h^{-1} for north-facing and 17.9 to 36.0 mm h^{-1} for south-facing plots. These steady-state infiltration rates are similar to other published rates from burned areas (probably without a well-defined ash layer), but are generally lower, which may be caused by the ash blocking the entry to mineral pores soil, attracting water to its surfaces, thereby preventing downward movement of water. However, all rates from burned areas fall within a narrow range of about one order of magnitude.

Three different theoretical spatial distribution models of i_∞ (threshold, modified threshold, and lognormal) were fit to the measurements of rainfall rate and steady-state discharge collected during 30-min rainfall simulations. This method provided estimates of the characteristics (mean, spatial variability, contribution area, and infiltration threshold) of the steady-state hydraulic conductivity within 1-m^2 plots on north- and south-facing hillslopes. Estimates of the mean or spatial-averaged, steady-state hydraulic conductivity ranged from 19.2 to 22.2 mm h^{-1}; the spatial variability quantified by the coefficient of variation (CV) ranged from 0.11 to 0.40 (lognormal model only); the contribution area ranged from 74% to 90% of the plot area (modified threshold model); and the rainfall or infiltration threshold ranged from 19.0 to 26 mm h^{-1}. These threshold estimates for 1-m^2 plots were about twice the published values for watersheds (0.5–100 km^2). This increase in threshold for smaller scales appears to be counter-intuitive, but probably reflects the water storage capacity of the ash.

Tensiometer measurements indicated a downward moving pressure wave and suggest that infiltration-excess overland flow is the runoff process on these burned hillslope with a two-layer system. Moreover, the results indicate that the ash layer is wettable, may block entry into the underlying layer, and increase the infiltration threshold; the underlying mineral soil, though coarser, limits the infiltration rate. The use of simple spatial distribution models in tandem with field measurements from rainfall simulations provided useful estimates for modeling purposes of the characteristics of the steady-state infiltration for a two-layer system. However, additional detailed field observations suggested that the infiltration variability is, not surprisingly, more complicated than the present spatial distribution models, and identified that processes like non-steady rainfall rates, runon, non-slope dependent wetting patterns, and spatial hydraulic connectivity of drainage networks must be investigated and incorporated into physically-based rainfall–runoff models for burned hillslopes.

Acknowledgments

Many people contributed to this work. Jonathan McKenna installed tensiometers in the field site. Jonathan Godt helped design the tensiometer experiments and provided clarification of issues related to two-layer soil systems. Wahab Sadeqi, Deborah Martin, and Joe Gartner provided field assistance during the experiments. Wahab also was instrumental in instrumentation development and testing, data verification, and field implementation. Several anonymous reviewers provided substantial comments, which were instrumental in improving the paper. The work was funded by a Mendenhall Post-Doctoral Fellowship for D. Kinner, and the USGS Landslide Hazards Program Wildfire and Debris Flow Project and National Research Program.

References

Anderson, H.W., 1974. Fire effects on water supply, floods, and sedimentation. In: Annual Proceedings 15th Tall Timbers Fire Ecology Conference, Pacific Northwest, October 16–17, 1974, vol. 15, pp. 249–260.

Benavides-Solorio, J., MacDonald, L.H., 2001. Post-fire runoff and erosion from simulated rainfall on small plots, Colorado Front Range. Hydrological Processes 15, 2931–2952.

Betson, R.P., 1964. What is watershed runoff? Journal of Geophysical Research 69, 1541–1552.

Birkeland, P.W., Shroba, R.R., Burns, S.F., Price, A.B., Tonkin, P.J., 2003. Soils and geomorphology in mountains – an example from the front range of Colorado. Geomorphology 55, 329–344.

Bolin, S.B., Ward, T.J., 1987. Recovery of a New Mexico drainage basin from a forest fire. In: Forest Hydrology and Watershed Management, Proceedings of the Vancouver Symp. vol. 167. IAHS Pub, pp. 191–198.

Brandt, T.R., Moore, D.W., Murray, K.E., 2003. A spatial database of bedding attitudes to accompany geologic map of the Boulder–Fort Collins–Greeley area, Colorado. In: Roger, B. (Ed.), Colton. US Geological Survey Open File Report 03-24.

Cannon, S.H., 2001. Debris-flow generation from recently burned watersheds. Environmental and Engineering Geoscience 7, 321–341.

Corradini, C., Morbidelli, R., Melone, F., 1998. On the interaction between infiltration and Hortonian runoff. Journal of Hydrology 204, 52–67.

Crockford, S., Topalidis, S., Richardson, D.P., 1991. Water repellency in a dry sclerophyll forest—measurements and processes. Hydrological Processes 5, 405–420.

Debano, L.F., 1981. Water repellent soils: a state-of the-art. Gen Tech Rep PSW-46, US Department of Agriculture Forest Service, Rocky Mountain Forest and Range Experimental Station, Berkeley, CA, pp. 1–21.

DeBano, L.F., 2000. The role of fire and soil heating on water repellency in wildland environments: a review. Journal of Hydrology 231–232, 195–206.

Dekker, L.W., Ritsema, C.J., 2000. Wetting patterns and moisture variability in water repellent Dutch soils. Journal of Hydrology, 148–164.

Doehring, D.O., 1968. The effect of fire on geomorphic processes in the San Gabriel Mountains, California. Contributions to Geology 7, 44–65.

Doerr, S.H., Moody, J.A., 2004. Hydrological effects on soil water repellency: on spatial and temporal uncertainties. Hydrological Processes 18, 829–832.

Doerr, S.H., Thomas, A.D., 2000. The role of soil moisture controlling water repellency: new evidence from forest soils in Portugal. Journal of Hydrology, 131–147.

Doerr, S.H., Shakesby, R.A., Walsh, R.P.D., 2000. Soil water repellency: its causes, characteristics and hydro-geomorphological significance. Earth-Science Reviews 51, 33–65.

Dunne, T., Dietrich, W.E., 1980. Experimental study of Horton overland flow on tropical hillslopes. Z. Geomorph. N.F. (Suppl.-Bd 3), 40–89.

Dunne, T., Zhang, W., Aubry, B.F., 1991. Effects of rainfall, vegetation and microtopography on infiltration and runoff. Water Resources Research 27, 2271–2285.

Eaton, E.C., 1935. Flood and erosion control problems and their solution. American Society of Civil Engineers Transactions 101, 1302–1362.

Fiedler, F.R., Ramirez, J.A., 2000. A numerical method for simulating discontinuous shallow flow over an infiltrating surface. International Journal for Numerical Methods in Fluids 32, 219–240.

Hawkins, R.H. 1982. Interpretations of source area variability in rainfall–runoff relations, water resources. In: Rainfall–Runoff Relationship, Proceedings of the International Symposium of Rainfall–Runoff Modeling, Mississippi State University, Starkville, Mississippi, pp. 303–324.

Hawkins, R.H., Cundy, T.W., 1987. Steady-state analysis of infiltration and overland flow for spatially-varied hillslopes. Water Resources Bulletin 23, 251–256.

Helvey, J.D., 1980. Effects of a north central Washington wildfire on runoff and sediment production. Water Resources Bulletin 16, 627–634.

Hershfield, D.M., 1961. Rainfall frequency atlas of the United States for duration from 30 minutes to 24 hours and return periods from 1 to 100 years. US Department of Commerce, Technical Paper No. 40, pp. 1–107.

Imeson, A.C., Verstraten, J.M., van Mulligen, E.J., Sevink, J., 1992. The effects of fire and water repellency on infiltration and runoff under Mediterranean type forest. Catena 19, 345–361.

Inbar, M., Tamir, M., Wittenberg, L., 1998. Runoff and erosion processes after a forest fire in Mount Carmel, a Mediterranean area. Geomorphology 24, 17–33.

Jarmillo, D.F., Dekker, L.W., Ritesma, C.J., Hendrickx, J.M.H., 2000. Occurrence of soil water repellency in arid and humid climates. Journal of Hydrology, 105–111.

Jones, T.P., Chaloner, W.G., Kuhlbusch, T.A.J., 1997. Proposed bio-geological and chemical based terminology for fire-altered plant matter. In: Clark, J.S., Cachier, H., Goldammer, J.G., Stocks, B. (Eds.), Sediment Records of Biomass Burning and Global Change. Spriner-Verlag, Berlin, pp. 9–22.

Kinner, D.A., Moody, J.A., 2005. Drainage networks after wildfire. International Journal of Sediment Research 20, 194–201.

Kinner, D.A., Moody, J.A., 2008. Infiltration and runoff measurements on steep burned hillslopes using a rainfall simulator with variable rainfall intensities. US Geological Survey Scientific Research Investigations Report 2007-5211.

Krammes, J.S., Rice R.M., 1963. Effect of fire on the San Dimas experimental forest. In: Arizona Watershed Symposium, Proceedings of the 7th Annual Meeting, Phoenix, Arizona, pp. 31–34.
Kunze, M.D., Stednick, J.D., 2006. Streamflow and sediment yield following the 2000 Bobcat Fire, Colorado. Hydrologic Processes 20, 1661–1681.
Letey, J., 2001. Causes and consequences of fire-induced water repellency. Hydrological Processes 15, 2867–2875.
Lu, N., Likos, W.J., 2004. Unsaturated Soil Mechanics. John Wiley, Hoboken, New Jersey.
MacDonald, L.H., Huffman, E.L., 2004. Post-fire soil water repellency: persistence and soil moisture thresholds. Soil Science Society of America Journal 68, 1729–1734.
Martin, D.A., Moody, J.A., 2001. Comparison of soil infiltration rates in burned and unburned mountainous watersheds. Hydrological Processes 15, 2893–2903.
Moody, J.A., Kinner, D.A., 2006. Spatial structure of stream and hillslope drainage structures following gully erosion after wildfire. Earth Surface Processes and Landforms 31, 319–337.
Moody, J.A., Martin, D.A., 2001a. Hydrologic and sedimentologic response of two burned watersheds in Colorado. US Geological Survey Water Resources Investigation Report 01-4122, pp. 1–142.
Moody, J.A., Martin, D.A., 2001b. Initial hydrologic and geomorphic response following a wildfire in the Colorado Front Range. Earth Surface Processes and Landforms 26, 1049–1070.
Moody, J.A., Martin, D.A., 2001c. Post-fire, rainfall intensity-peak discharge relations for three mountainous watersheds in the western USA. Hydrological Processes 15, 2981–2993.
Moody, J.A., Martin, D.A., Haire, S.L., Kinner, D.A., 2008. Linking runoff response to burn severity after a wildfire. Hydrological Processes 22 (13), 2063–2074.
Moody, J.A., Kinner, D.A., Ubeda, X., 2009. Linking hydraulic properties of fire-affected soils to infiltration and water repellency. Journal of Hydrology 379, 291–303.
Morel-Seytoux, H.J., 1986. Influence of variability in hydraulic conductivity on hillslope infiltration. In: Proceedings 6th Annual AGU Hydrology Days, Hydrology Days, Fort Collins, CO. Hydrology Day Publications. Atherton, CA, pp. 153–170.
Nachabe, M.H., Illangaskeare, T.H., Morel-Seytoux, H.J., Ahuja, L.R., Ruan, H., 1997. Infiltration over heterogeneous watershed: influence of rain excess. Journal of Hydrologic Engineering 2, 140–143.
Neary, D.G., Klopatek, C.C., DeBano, L.F., Ffolliott, P.F., 1999. Fire effects on belowground sustainability: a review and synthesis. Forest Ecology and Management 122, 51–71.
Onda, Y., Dietrich, W.E., Booker, F., 2008. Evolution of overland flow after a severe forest fire, Point Reyes, California. Catena 72, 13–20.
Parrett, C., 1987. Fire-related debris flows in the Beaver Creek drainage, Lewis and Clark County, Montana. US Geological Survey Water Supply Paper 2330, pp. 57–67.
Poesen, J.W.A., 1993. Mechanism of overland-flow generation and sediment production on loamy and sand soils with and without rock fragments. In: Parson, A.J., Abrahams, A.D. (Eds.), Overland Flow Hydraulics and Erosion Mechanics. Chapman & Hall, New York, pp. 275–305.
Robichaud, P.R., 2000. Fire effects on infiltration rates after prescribed fire in Northern Rocky Mountain forests, USA. Journal of Hydrology, 220–229.
Römkens, M.J.M., Prasad, S.N., Whisler, F.D., 1990. Surface sealing and infiltration. In: Anderson, M.G., Burt, T.P. (Eds.), Process Studies in Hillslope Hydrology. John Wiley, New York, pp. 127–172.
Ross, B., 1990. The diversion capacity of capillary barriers. Water Resources Research 26, 2625–2629.
Rowe, P.B., 1948. Influence of woodland chaparral on water and soil in central California, California State Board of Forestry, Sacramento, 70 p.
Scott, D.F., van Wyk, D.B., 1990. The effects of wildfire on soil wettability and hydrological behaviour of an afforested catchment. Journal of Hydrology 121, 239–256.
Shakesby, R.A., Doerr, S.H., 2006. Wildfire as a hydrological and geomorphological agent. Earth-Science Reviews 74, 269–307.
Smith, R.E., 1990. Analysis of infiltration through a two layer soil profile. Soil Society of America Journal 54, 1219–1227.
Smith, R.E., Goodrich, D.C., 2000. Model for rainfall excess patterns on randomly heterogeneous areas. Journal of Hydrologic Engineering 5, 355–362.
Sumner, M.E., Stewart, B.A. (Eds.), 1992. Soil Crusting: Chemical and Physical Processes. CRC Press, Inc., Boca Raton, Florida.
Trabaud, L., 1994. The effect of fire on nutrient losses and cycling in a *Quercus coccifera* garrigue (southern France). Oecologia 99, 379–386.
Veenhuis, J.E., 2002. Effects of wildfire on the hydrology of Capulin and Rito De Los Frijoles Canyons, Bandalier National Monument, New Mexico. US Geological Survey Water-Resources Investigation Report 02-4152.
Wang, Z., Wu, Q.J., Wu, L., Ritsema, C.J., Dekker, L.W., Feyen, J., 2000. Effects of soil water repellency on infiltration rate and flow instability. Journal of Hydrology, 265–276.
Wondzell, S.M., King, J.G., 2003. Postfire erosional processes in the Pacific Northwest and Rocky Mountain regions. Forest Ecology and Management 178, 75–87.